

SCIENTIFIC REPORTS



OPEN

A new nanoscale metastable iron phase in carbon steels

Tianwei Liu^{1,5}, Danxia Zhang², Qing Liu³, Yanjun Zheng¹, Yanjing Su², Xinqing Zhao³, Jiang Yin⁴, Minghui Song⁵ & Dehai Ping⁵

Received: 01 April 2015

Accepted: 23 September 2015

Published: 27 October 2015

Metastable ω phase is common in body-centred cubic (bcc) metals and alloys, including high-alloying steels. Recent theoretical calculations also suggest that the ω structure may act as an intermediate phase for face-centred cubic (fcc)-to-bcc transformation. Thus far, the role of the ω phase played in fcc-bcc martensitic transformation in carbon steels has not been reported. In previous investigations on martensitic carbon steels, extra electron diffraction spots were frequently observed by transmission electron microscopy (TEM), and these spots were historically ascribed to the diffraction arising from either internal twins or carbides. In this paper, an intensive TEM investigation revealed that the extra spots are in fact attributed to the metastable ω phase in particle-like morphology with an overall size of several or dozens of nanometres. The strict orientation relationships between the ω phase and the ferrite matrix are in good agreement with those of the hexagonal (P6/mmm) ω phase in other bcc metals and alloys. The identification of the ω phase as well as the extra diffraction spots might provide a clue to help understand the physical mechanism of martensitic transformation in steels.

It has long been known that the rapid quenching of carbon steels can lead to the formation of a very hard phase, martensite, and its outstanding hardness has been recognized to arise from the supersaturated carbon in ferrite formed by a diffusionless martensitic transformation in which the carbon—formerly in face-centred cubic (fcc) austenite—remains in the bcc martensite. Because of its vital importance to metallurgical engineering and academic research in solid-state physics, the above fcc-to-body-centred cubic (bcc) transformation has received persistent attention since the 1920s, and voluminous experimental work as well as theoretical considerations can be found in the literature^{1,2}. Nevertheless, because of the complexity of martensitic transformations in steels with different compositions, a convincing theory has not satisfactorily demonstrated the specific transformation process, particularly the mechanism for lattice transition from fcc to bcc. A prevailing crystallographic theory of the martensitic transformation—also called the phenomenological theory—was proposed in the 1950s based on the Bain strain model, and an assumption was made that the interface between austenite and martensite is undistorted at a macroscopic scale. Although the phenomenological theory has been successfully applied to describe the crystallographic characteristics—such as the shape deformation, the orientation of the habit plane and the orientation relationship between parent and product phases^{1,2}—it is not applicable to elucidating the mechanism underlying the displacement and shuffling of atoms during martensitic transformation in steels. For example, the (225) and (259) habit planes observed in certain high-carbon Fe-C and Fe-Ni-C steels cannot be explained by a single (112) twinning system in martensitic variants predicted by the phenomenological theory^{3–5}.

The complexity of martensitic transformation in steels has long been recognized to be closely associated with the existence of carbon because carbon can exert a significant influence on the properties of

¹Department of Materials Science and Engineering, China University of Petroleum, Beijing 102249, China. ²School of Materials Science and Engineering, University of Science and Technology Beijing, Beijing 100083, China. ³School of Materials Science and Engineering, Beihang University, Beijing 100191, China. ⁴Jiangsu Asian Star Anchor Chain Co. Ltd., Jingjiang 214533, China. ⁵National Institute for Materials Science, Sengen 1-2-1, Tsukuba 305-0047, Japan. Correspondence and requests for materials should be addressed to Y.J.Z. (email: zhengyj@cup.edu.cn) or X.Q.Z. (email: xinqing@buaa.edu.cn) or D.H.P. (email: Ping.de-hai@nims.go.jp)

martensite, such as its hardness, morphologies and substructures. The morphology of the martensites in carbon steels is always observed in two distinctly different types depending on the content of carbon: lath martensite in low-carbon steels and lenticular martensite in high-carbon steels. Twins, often observed as a substructure of martensite in high-carbon steels, were confirmed to be of the $\{112\}\langle 111\rangle$ type and considered to be similar to other bcc metals and alloys^{6–10}; dislocations are observed to be characteristic of martensitic substructure in low-carbon steels^{3–5}. It is worth noting that during TEM observations, extra diffraction spots at the positions of $1/3\{112\}$ and $2/3\{112\}$ were invariably observed in the diffraction patterns from the martensitic $[110]_{\text{bcc}}$, $[113]_{\text{bcc}}$, and $[120]_{\text{bcc}}$ zone axes, and these extra diffraction spots were attributed to the double diffraction of the twins in some studies^{11–16}. However, the same diffraction patterns with extra spots were also found in martensitic steel comprising lath martensite with dislocations as its substructure. In this case, some researchers considered the extra diffraction spots to have arisen from carbides^{17–20}. Obviously, these different explanations for the same extra diffraction spots in different types of martensitic steels are contradictory. Clarifying the origin of the extra diffraction spots in martensitic steels is helpful to understanding the mechanism of the martensitic formation and involution process.

Very recently, Ping *et al.* noticed that the extra diffraction spots in commercial spring steel with medium carbon content can be indexed by an ω phase²¹ a metastable phase commonly existing in other bcc metals and alloys^{22–24}. Theoretical calculations also suggested that carbon is a stabilizing element for the ω phase in steels²¹. Very recent investigations of the phase transition pathway by first-principles calculations showed that the ω structure appears during the fcc-bcc transformation²⁵, and the phase transformation follows a route of fcc- ω -bcc or fcc- ω +bcc^{25,26}. Studies on the martensitic transformation in steels have been conducted for almost one hundred years. If the ω structure is a prior phase to martensite, it must have left traces, whereas current observation and analysis are able to exploit the increased power of modern instrumentation. In the present study, we strictly exclude certain other possible explanations for the extra spots in diffraction patterns, such as double diffraction of twinning or diffraction of carbide, and confirm that the extra spots can be attributed to the ω phase. It is expected that the metastable phase will provide a clue in searching for a physical explanation of the mechanism of martensitic transformation in steels.

Results

Figure 1(a,b) depict a typical bright-field TEM image and its corresponding selected area electron diffraction (SAED) pattern of martensite with internal twins as a substructure in the as-quenched Fe-0.58 mass% C sample, respectively. The dashed circle in Fig. 1(b) indicates a twin spot in addition to the normal bcc $[011]$ zone diffraction spots, and two arrows indicate extra spots at $1/3(\bar{2}1\bar{1})$ and $2/3(\bar{2}1\bar{1})$ in addition to the matrix and twin diffraction patterns. The dark-field TEM image shown in Fig. 1(c) was captured using the diffraction spot outlined by the dashed circle in Fig. 1(b). It was generally believed that the twin boundary planes in metallic materials should be straight or sharp even at the atomic level^{4,27}. However, it is interesting to note that the twins or twin boundaries are curved in the dark-field image (Fig. 1(c)) with higher magnification, although they seem straight in the bright image with lower magnification.

Figure 1(d) shows a high-resolution TEM lattice image of the $\{112\}\langle 111\rangle$ twins in Fig. 1(a). One can see clearly that the width of the matrix is almost identical to that of the twin parts. The twinning boundaries are indeed not sharp at the atomic level, consisting of “interrupted” or “overlapped” atomic layers. Obviously, these interrupted or overlapped twinning boundaries are controversial with the conventional twinning mechanism for martensite—i.e., shear mechanism. On the basis of the conventional twinning mechanism, the twinning boundaries should be atomically sharp and straight if the incident electron beam is parallel with the twinning zone axes, such as the case shown in Fig. 1(b). In the present study, a large number of high-resolution TEM observations on the twinning boundaries were made, and almost all twinning boundaries were not straight at the atomic level.

In addition to the diffraction spots from the matrix and twin crystals, the extra spots—as indicated by arrows in Fig. 1(b)—also exist. In previous studies of martensitic steels, such extra diffraction spots were frequently observed and were usually treated as spots arising from double diffraction by the $\{112\}\langle 111\rangle$ twinning structure^{11–16}. According to electron diffraction theory, double diffraction is a dynamical effect whereby electrons that have been Bragg diffracted by one crystal satisfy the Bragg condition for another¹⁵. Thus, double diffraction can occur when the electron beam is diffracted by twins in a crystal structure, but does not occur in a single crystal with a disordered cubic structure. Indeed, theoretical treatment of the double diffraction of twinning in bcc and fcc lattices has indicated that double diffraction can occur in $\{111\}_{\text{fcc}}\{112\}_{\text{bcc}}$ systems^{14,15}. In these theoretical treatments, the matrix is regarded as the first crystal and the twin as the second crystal. Previous studies^{13,28,29} have explained these extra spots as double diffraction that can occur when the size of the twins is at the nanoscale and the observed region is sufficiently thick to contain several twins in the depth direction. Nonetheless, if the incident electron beam is parallel with the twinning boundary plane and there is no overlap between the matrix and the twin in the depth direction, it is normally impossible to observe any double diffraction in the twinning diffraction pattern.

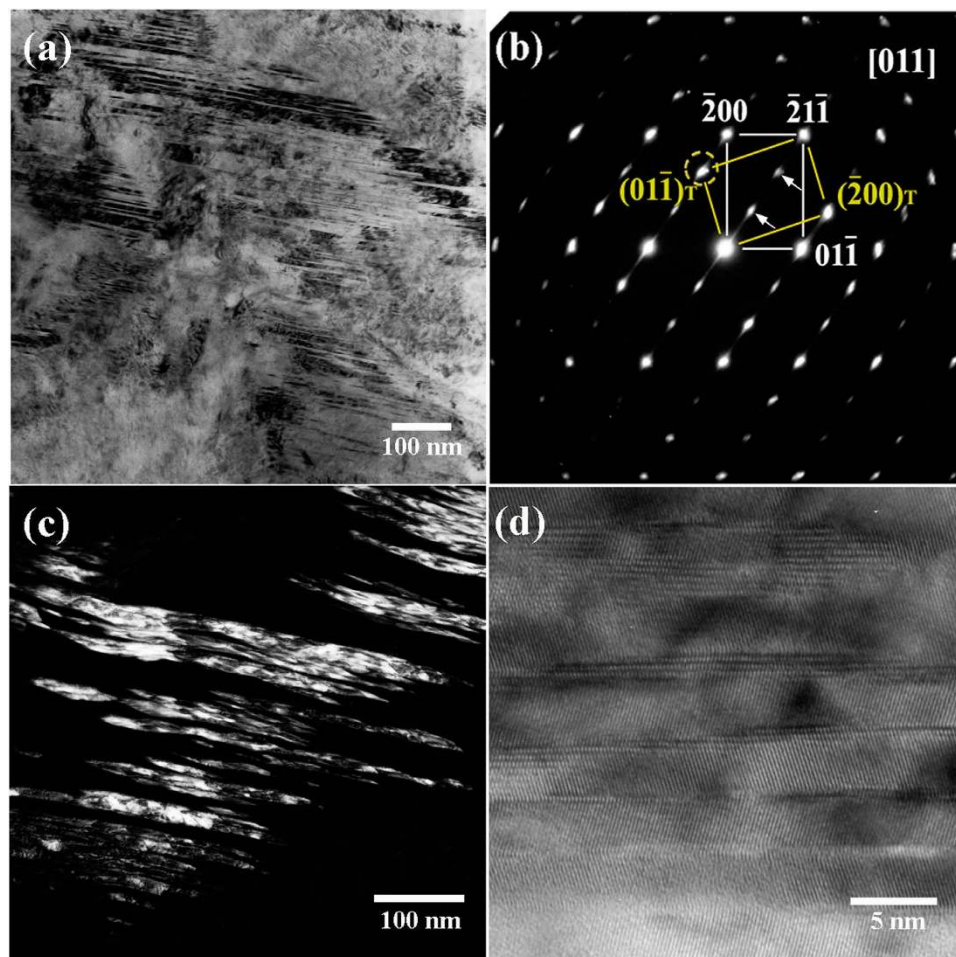


Figure 1. TEM results from the as-quenched Fe-0.58 mass% C sample. (a) Bright-field micrograph revealing a high density of twins in the martensite. (b) The corresponding SAED pattern with a $\{112\}\langle 111\rangle$ -type twinning structure observed together with the ω phase. (c) The dark-field micrograph imaged using the diffraction spot outlined by the dashed circle in (b). (d) A high-resolution TEM lattice image of the $\{112\}\langle 111\rangle$ twins together with the ω phase at the twinning boundaries.

To clarify the dynamic diffraction pattern in a bcc twin system, xHREM (a software for calculating high-resolution TEM image, developed by HREM Research Inc., at Higashimatsuyama 355-0055, Japan) was employed to perform a dynamic calculation on the bcc $\{112\}\langle 111\rangle$ -type twinning. Figure 2 represents a $\{112\}\langle 111\rangle$ -type twinning unit cell for the calculation with $a=0.2482$ nm, $b=9.83$ nm, $c=0.4054$ nm and a twinning plane in the middle. Such a unit cell consists of a bcc $\{112\}\langle 111\rangle$ -type twinning structure. During the calculation, the software generated an arbitrary repeat of the unit cell periodically along its a and b axes. In this situation, another twinning plane exists at the end of the cell because the unit cell is under a periodic boundary condition. The electron beam is parallel with the c axis, and a partial projection along the $[110]_{\text{bcc-Fe}}$ direction is shown in Fig. 2(b). All atoms can be seen in a small-scaled map as shown in Fig. 2(c). Figure 2(d) shows three twinning unit cells projected along the $[110]$ direction.

The calculated dynamic twinning diffraction patterns with several different thicknesses along the $[110]$ zone axis are shown in Fig. 3. The twinning unit cell is repeated along $[1\bar{1}2]$ during calculation; therefore, the twinning plane—which can be regarded as “a plane defect”—is also repeated and has a periodic distribution along the same direction. When the thickness is approximately 4 nm, the diffraction spots are in a regular twinning pattern; however, some weak dots or streaking between spots $1\bar{1}0_{\text{twin}}$ and 002 can be seen in Fig. 3(a). These weak spots or streaking are most likely caused by the super-lattice property of the twinning plane constructed in the present calculation. Because these super-lattice spots will change their position if the periodic distance of the constructed twinning plane changes—in reality, the twin plane distance is not constant, varies randomly and thus does not even produce any super-lattice spots—these super-lattice spots appearing in the calculation might not be responsible for the “double diffraction spots”. When the thickness is increased to 80 nm—which is normally a comparable thickness

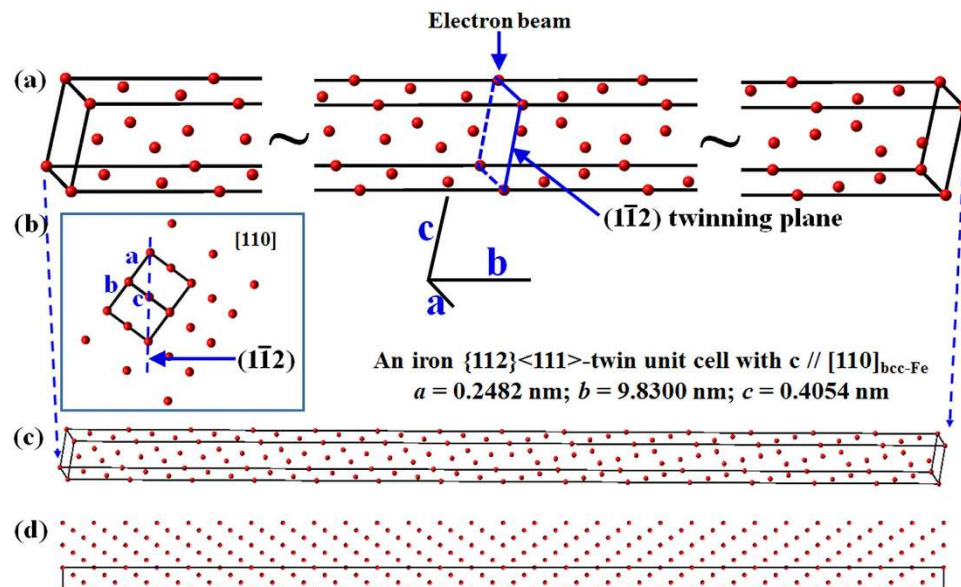


Figure 2. (a) Parts of the constructed unit cell; the whole twinning unit cell with $a = 0.2482 \text{ nm}$, $b = 9.83 \text{ nm}$ and $c = 0.4054 \text{ nm}$. (b) Two-dimensional atom configuration of bcc structure projected along the $[110]$ direction. (c) A smaller scale of (a) showing all the atoms in one twinning unit cell. The constructed $\{112\}\langle 111\rangle$ -type twin has 84 atoms, and the twinning plane is in the middle and the end of the cell. (d) The projected atom configuration of three twinning unit cells along $[110]$.

to that in the TEM observation region—a very strong line—which can be many strong spots connected to one another—appears between spots A and B, as shown in Fig. 3(d). Such strong lines have never been observed during experimental observations. From Fig. 3(a) through (d), in addition to these super-lattice spots, the so-called “double diffraction spots” of the $\{112\}\langle 111\rangle$ -type twinning structure cannot be observed, regardless of the sample thickness. Thus, the interpretation of the extra spots in terms of double diffraction could not provide any evidence from the present dynamic calculation.

For further investigation of the extra spots appearing in the electron diffraction of martensites, diffraction patterns from various zone axes were recorded. Figure 4(a,b) show the SAED pattern of the $[\bar{1}12]_{\alpha}$ zone axis and the corresponding bright-field TEM image of the as-quenched Fe-0.58 mass% C sample, respectively. The pattern shown in Fig. 4(a) clearly reveals two sets of diffraction spots. One set with strong spots is from α -ferrite, whereas the other set of weak spots can be seen at the positions of $1/3(\bar{2}2\bar{2})$ and $2/3(\bar{2}2\bar{2})$. These extra spots cannot be treated as “double diffraction” of the $\{112\}\langle 111\rangle$ -type twinning structure because the twinning plane is $\{112\}$, which is perpendicular to the incident electron beam. In such cases, all matrices and twins will result in exactly the same diffraction spots and the diffraction patterns should be totally overlapped. Obviously, these extra weak diffraction spots must arise from another unknown crystalline phase. Tilting the diffraction pattern about the $[110]$ direction in Fig. 4(a) approximately 20° produced the $[\bar{1}11]$ zone axis of α -Fe. The SAED pattern of the $[\bar{1}11]_{\alpha}$ zone axis and the corresponding bright-field TEM image are shown in Fig. 4(c,d), respectively. In this case, the extra spots cannot be observed, suggesting that the unknown phase possesses a specific orientation with α -Fe. In some early literature, the extra diffraction spots were indexed as ϵ carbide or a type of cementite^{17–20}. Based on the structure parameters of well-known carbides^{30,31}, we confirmed that these extra diffraction spots cannot be indexed as any well-known carbide. Taking ϵ carbide for example, it is well documented that it has the orientation relationship $[\bar{1}11]_{\text{bcc}} // [1\bar{1}\bar{2}0]_{\epsilon}$, $(011)_{\text{bcc}} // (0001)_{\epsilon}$ ^{32–38}. However, when the martensite plate is tilted to the $[100]$ or $[111]$ zone axis, no diffraction spots other than the fundamental bcc diffraction spots were observed. This finding suggests that the extra diffraction spots are not from ϵ carbide or any other type of carbide.

To confirm the universality of the existing specific phase that contributes the extra diffraction spots in martensitic carbon steels, an Fe-0.98 mass% C binary alloy was selected for further TEM observations. Figure 5 shows the TEM observation results of the specimen in an as-quenched state. The TEM foil for observation is taken from the middle part of the quenched plate specimen with 0.5 mm in thickness. It can be seen from a typical bright-field TEM micrograph and the corresponding SAED pattern shown in Fig. 5(a) that the observed region contains several martensitic crystal grains with different orientations, and there is no clear evidence of a twin substructure. Figure 5(b) depicts a high-magnification image of the region outlined by the dashed rectangle in Fig. 5(a). It should be noted that unambiguous contrast at the nanometre scale was observed, suggesting that the plate martensite seemingly has an

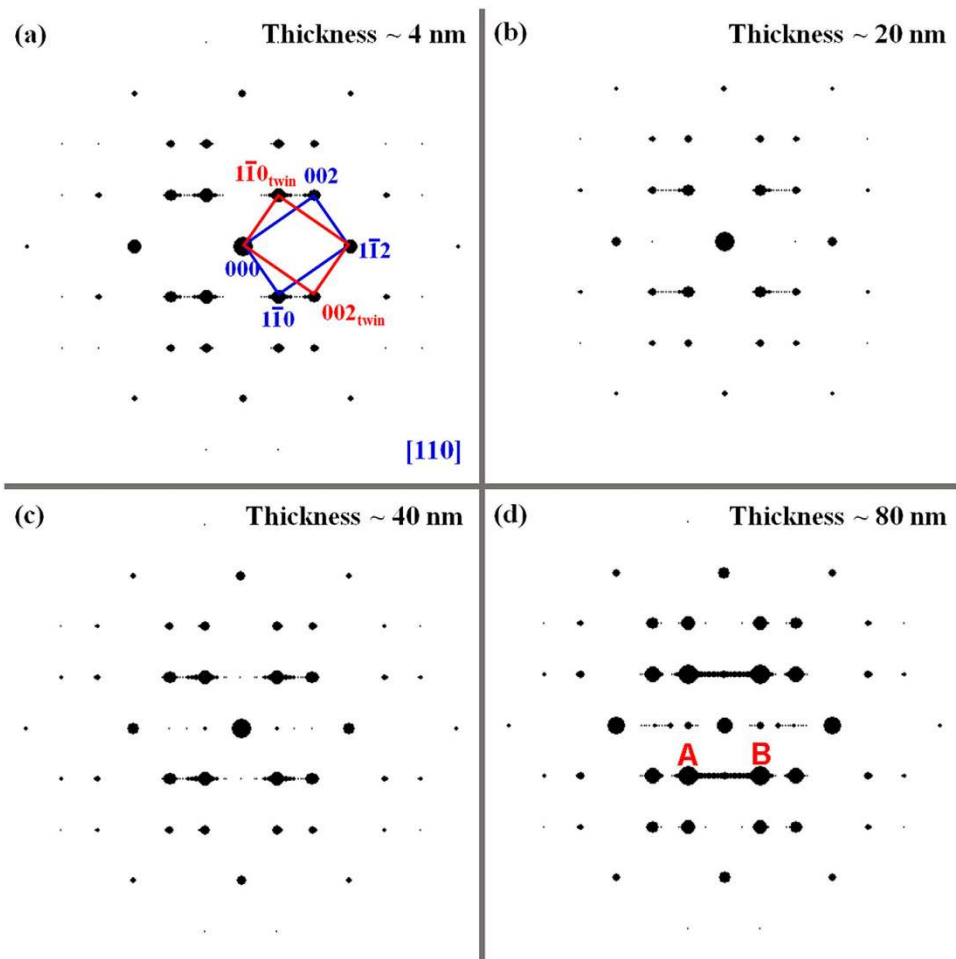


Figure 3. Calculated diffraction patterns of a $\{112\}\langle 111\rangle$ -type twinning structure with various thickness. The dashed spots along the $[1\bar{1}2]$ direction are caused by the super-lattice structure of the twinning interface during calculation because the twinning unit cell was repeated many times to increase the thickness and width.

extra substructure rather than a homogenous single phase. To verify the substructure, an intensive diffractometric analysis was performed. Figure 5(c,d) depict the dark-field images by the extra diffraction spots denoted as *c* and *d* shown in Fig. 5(a), respectively. The dark-field images reveal clearly that a high density of ultrafine particles exists in the plate martensite, and no trace of twinned substructure was directly observed in the present study.

Figure 6(a) shows a high-resolution TEM lattice image of the above ultra-fine particles in the plate martensite. The corresponding Fourier-filtered transformed (FFT) diffraction pattern and the inversed FFT lattice image are shown in Fig. 6(b,c), respectively. Figure 6(b) clearly indicates that the diffraction pattern is composed of two sets of sub-patterns wherein one set is indexed as $bcc\text{-Fe}$ or ferrite phase. Considering the fact that no twinning contrast could be observed in the region from the bright, dark and high-resolution TEM observations, the other set of patterns at $1/3(\bar{2}1\bar{1})_{bcc}$ and $2/3(\bar{2}1\bar{1})_{bcc}$, indicated by white arrows in Fig. 6(b), could be ascribed to another specific phase. Again, calculations using parameters of carbides do not achieve a similar result to that shown in Fig. 6(b). From the inverse FFT high-resolution TEM image shown in Fig. 6(c), one can clearly observe local regions with different lattice contrasts, as outlined by the white circle. Obviously, this nanometre-sized region can be attributed only to a specific phase.

Researchers have employed another approach to interpreting the extra spots in diffraction patterns. It is well known that groups of martensite variants form in a single austenite grain during martensitic transformation to accommodate the huge transformation strain. Therefore, there must be pairs of martensite variants with a twin-orientation relationship within a single austenite grain^{39,40}. If some martensitic variants are sufficiently thin, their diffraction spots in the reciprocal space may elongate and produce high-order Laue spots if the elongated spots are sufficiently long to intersect the Ewald sphere. Twin-effect-induced high-order Laue spots have been confirmed in some materials⁴¹. However,

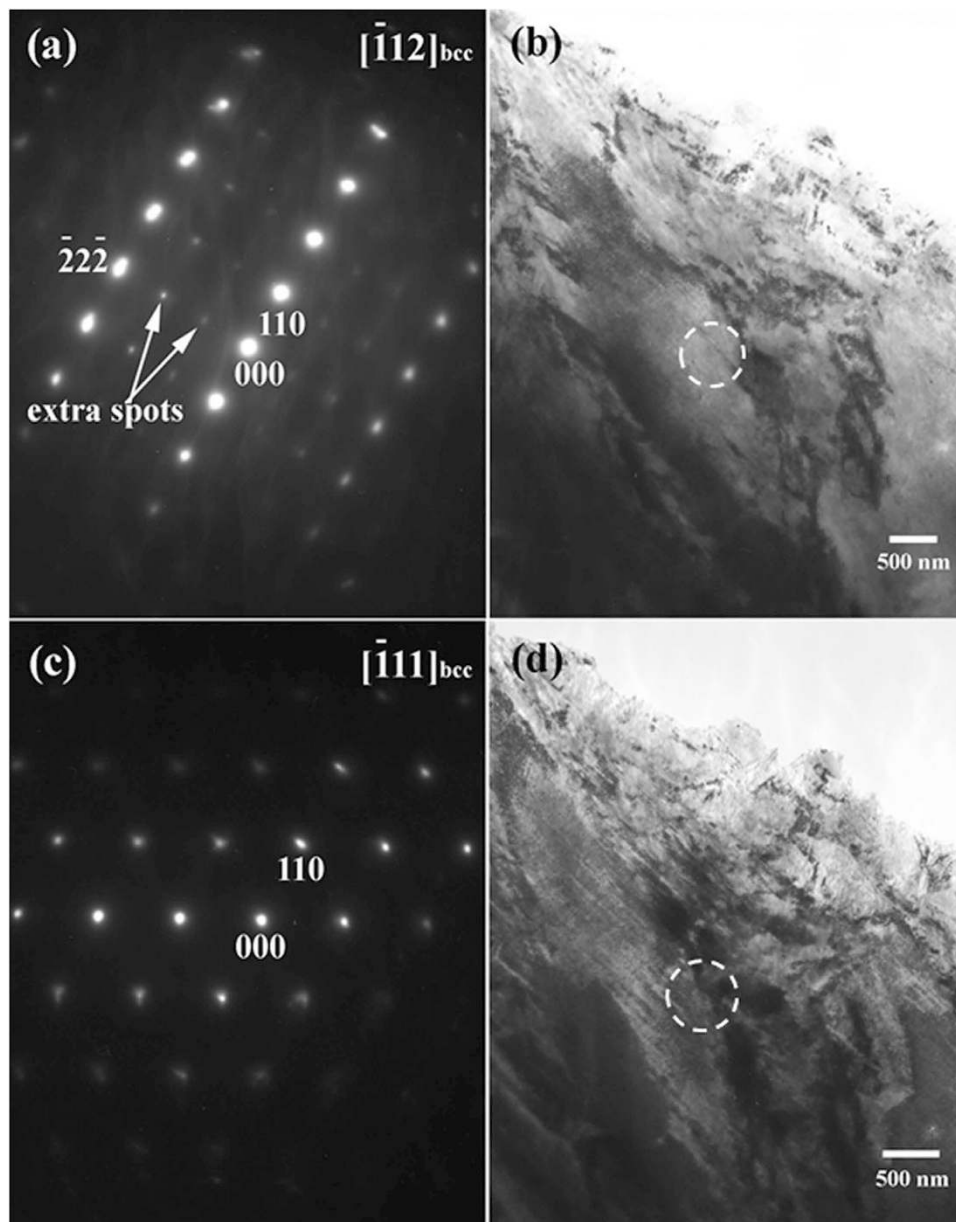


Figure 4. The SAED patterns of $[\bar{1}12]_{\alpha}$ and $[\bar{1}11]_{\alpha}$ zone axes and their corresponding bright-field TEM images of the as-quenched Fe-0.58 mass% C sample, respectively. (a,b) are the SAED pattern from α -Fe with the $[\bar{1}12]_{\alpha}$ zone axis parallel to the incident electron beam and the corresponding bright-field TEM image in which the SAED pattern was taken from the circled region. (c,d) are the SAED pattern from the $[\bar{1}11]_{\alpha}$ zone axis after tilting (a) approximately 20° and the corresponding bright-field TEM image in which the SAED pattern was taken from the circled region.

our calculation shows that the streaking of reciprocal spots does not produce the same diffraction pattern—for example, the pattern shown in Fig. 4(a).

Furthermore, the subsequent dark-field image observation does not suggest that the extra spots result from merely martensite variants themselves. In Fig. 5, the dark-field images show that the extra spots result from a crystal region several or dozens of nanometres in size. Until now, there has been no report or theoretical analysis claiming that martensite contains substructure at the nanometre scale. The same is true for twinning-structured martensite. Figure 7 shows a typical bright-field TEM image of a twinned region in the as-quenched Fe-0.58 mass% C sample. The corresponding SAED pattern with twinning structure is shown in Fig. 7(b). Figure 7(c,d) are the dark-field images using the diffraction spots “c” and “d” shown in Fig. 7(b), respectively. One can find many bright dots at the nanometre scale scattered along the twin boundary from the dark-field image shown in Fig. 7(d). To the knowledge of the present

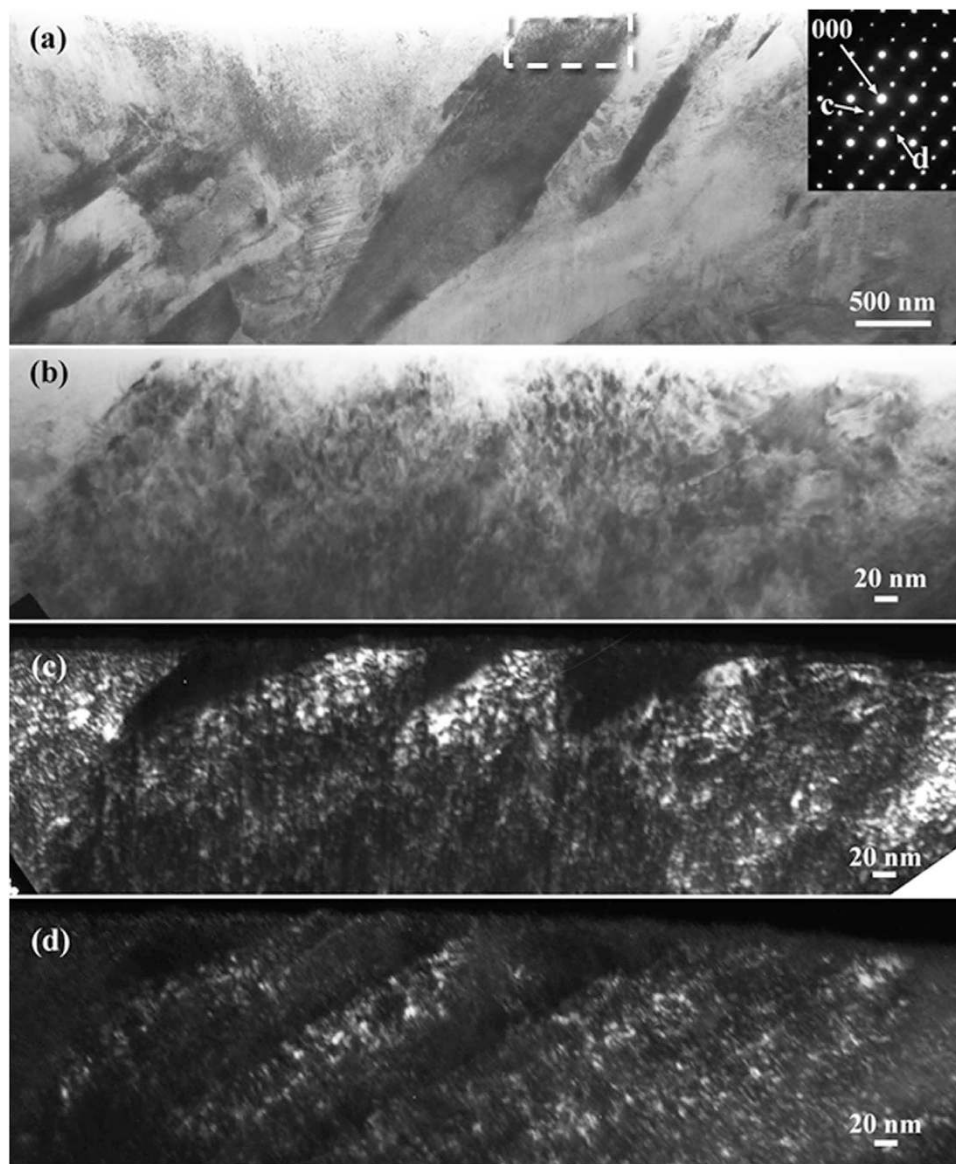


Figure 5. TEM observation results from the as-quenched Fe-0.98 mass% C sample. (a) A typical bright-field image of plate martensite and the corresponding SAED pattern observed with the electron beam parallel to $[011]_{\text{bcc}}$. (b) High magnification of the region outlined by the dashed rectangle in (a). (c,d) are dark-field images of the diffraction spots *c* and *d* in (a), respectively.

authors, previous research on conventional martensitic transformation did not predict or consider the presence of these nano-sized regions in Fig. 7(d) or the nano-sized regions in Fig. 5.

Discussion

Many experimental investigations have demonstrated that a metastable phase, designated as ω , typically precipitates from the matrix of bcc metals and alloys when the bcc lattice becomes unstable by doping, high-speed impact or high pressure^{22,42–45}. Omega is a hexagonal structure with a space group of P6/mmm (191), which is different from that of a hexagonal close-packed structure, P6₃/mmc (194). Metastable ω phase is a common phase in Group IV metals and their alloys^{22–24}, such as β -type Ti (Zr or Hf) alloys, heavily deformed pure Mo⁴⁶, β -brass^{47,48}, Ta⁴⁹ and some Fe-based high alloys^{50,51}. The ω phase is always coherent with the bcc matrix with the lattice relationships of $a_{\omega} = \sqrt{2} \times a_{\text{bcc}}$ and $c_{\omega} = \sqrt{3}/2 \times a_{\text{bcc}}$, following the orientation relationships of $[\bar{1}13]_{\text{bcc}} // [\bar{1}\bar{1}23]_{\omega}$, $(110)_{\text{bcc}} // (\bar{1}011)_{\omega}$, and $(2\bar{1}1)_{\text{bcc}} // (1\bar{1}00)_{\omega}$. According to the mechanism for ω phase formation, the lattice can be obtained by collapsing one pair of $(111)_{\text{bcc}}$ planes and keeping the neighbouring $(111)_{\text{bcc}}$ plane unaltered within the bcc lattice^{49,52}.

Some researchers recently studied the phase-transition pathway by first-principles calculations, showing that the ω structure appears during the fcc-bcc transformation²⁵ and the phase transformation

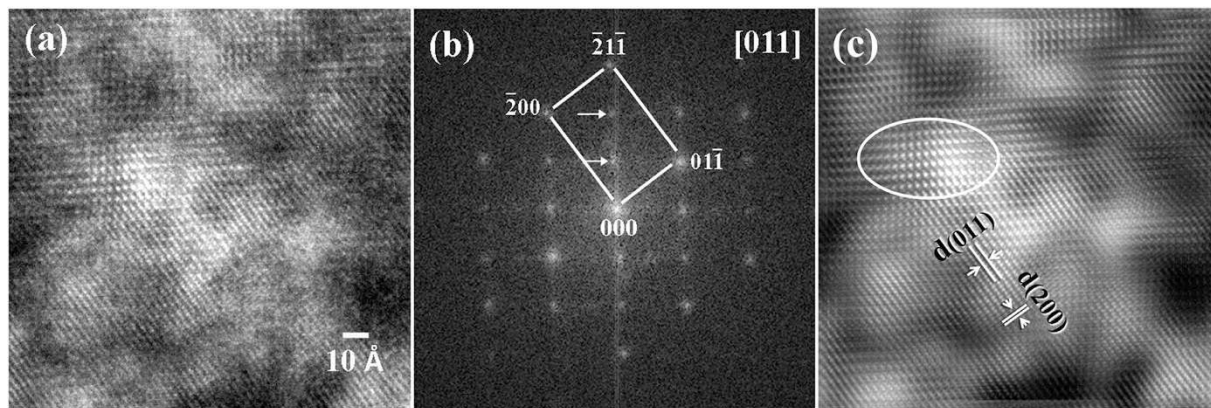


Figure 6. High-resolution TEM lattice image of ultra-fine particles in the plate martensite. (a) HRTEM lattice image revealing different lattice contrast. (b) Fourier-filtered transformed (FFT) diffraction pattern showing bcc-ferrite and extra spots. (c) Inverse FFT image of (a) displaying an HRTEM image with bcc and another lattice.

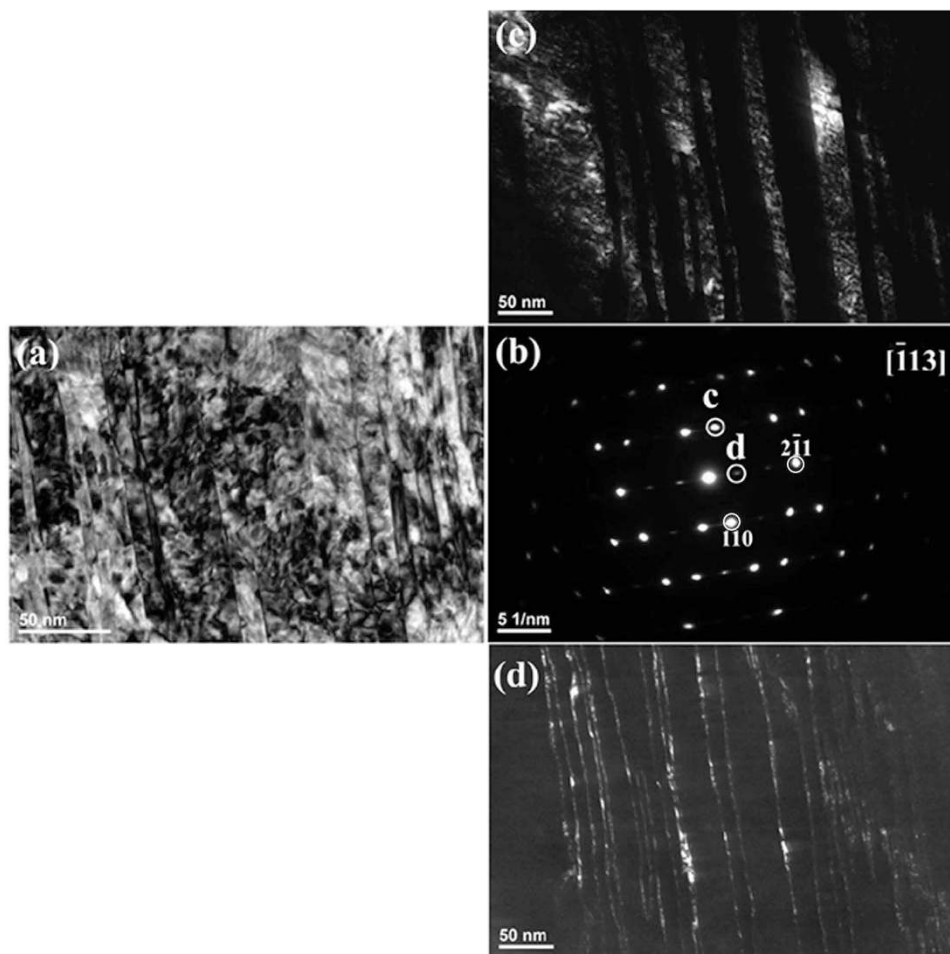


Figure 7. SAED patterns of $[\bar{1}13]_{\alpha}$ and the corresponding bright-field TEM images of the as-quenched Fe-0.58 mass% C sample. (a) The bright-field image; (b) the SAED pattern from α -Fe with $[\bar{1}13]_{\alpha}$ as the zone axis. (c,d) are the dark-field images taken from the spots shown in (b) indicated by circles “c” and “d”, respectively.

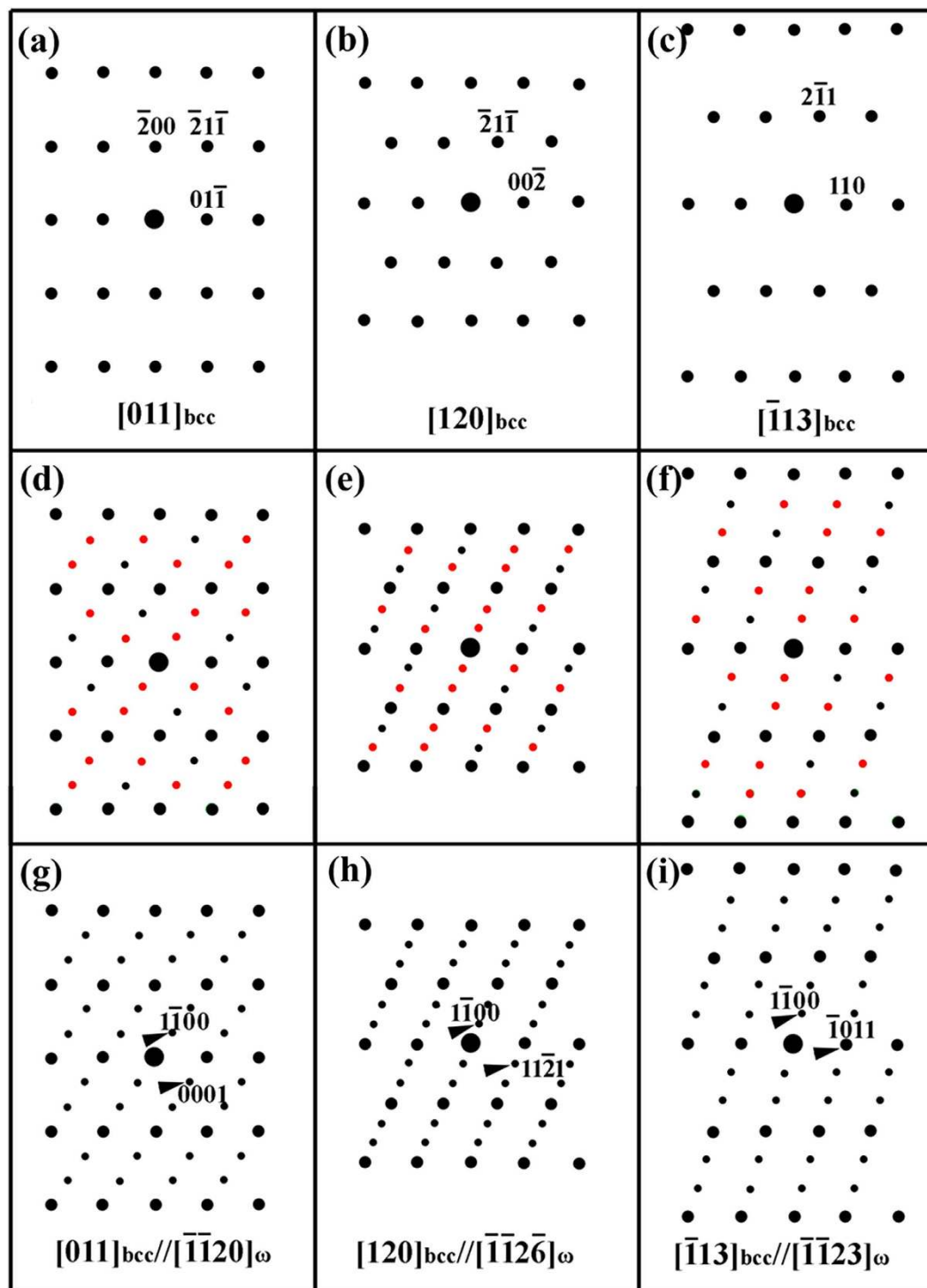


Figure 8. Schematic illustrations of the electron diffraction patterns with the electron beam parallel to the (a) $[011]$, (b) $[120]$ and (c) $[\bar{1}13]$ zone axes of a bcc single crystal observed on TEM. In (d–f), there are extra sets of diffraction spots in addition to the diffraction spots from the bcc crystal. The small black spots, including those overlapped with the larger black spots from the bcc crystal, have a $\{112\}\langle 111\rangle$ -type twinning relationship in the bcc crystals. Other small extra spots in red (colour online) were conventionally understood to be double-diffraction spots between matrix and twin. (g–i) are rebuilt by using ω phase parameter, where the diffraction spots are exactly the same as in (d–f).

follows fcc- ω -bcc or fcc- ω +bcc^{25,26}. Based on this evidence, it might be reasonable to suppose the existence of the ω phase in carbon steels. We recalculated the electron diffraction patterns of the bcc matrix by taking into account the ω phase. Figure 8 shows schematic illustrations of the electron diffraction

C	Si	Mn	Cr	Fe	M_s
0.58	1.60	0.58	1.10	bal.	521 K
0.98	0.25	0.33	1.50	bal.	406 K

Table 1. Chemical composition (mass%) and the calculated M_s temperatures^{57,58} of the steels investigated.

patterns with the electron beam parallel to the $[011]_{\text{bcc}}$ (Fig. 8(a)), $[120]_{\text{bcc}}$ (Fig. 8(b)) and $[\bar{1}13]_{\text{bcc}}$ (Fig. 8(c)) zone axes. Figure 8(d) through (f) show that there are extra sets of diffraction spots along with the diffraction spots from the bcc crystal. The small black spots—including those overlapping the larger black spots from the bcc crystal—have a $\{112\}\langle 111\rangle$ -type twinning relationship in bcc crystals. In addition, some extra small diffraction spots are highlighted in red (colour online). These extra spots were conventionally considered to be double-diffraction spots between the matrix and twin. In fact, if the ω phase is included in the calculation, the corresponding results could be rebuilt into Fig. 8(d) through (f) and the final diffraction patterns could be represented as Fig. 8(g) through (i). The calculated diffraction spots perfectly match the spots observed in 0.58% C and 0.98% C steels, with reference to Figs 1 and 4–6. For example, the TEM morphologies of the quenched 0.98% C specimen shown in Fig. 5 could be considered important evidence that the extra diffraction spots are not from the double diffraction of twinning but, rather, from a specific phase.

Very recently, an ω -lattice mechanism was proposed to explain the formation of $\{112\}\langle 111\rangle$ twinning from nanoscale metastable ω precursors⁵³, providing a helpful perspective for understanding the results achieved in the present study. On the basis of the proposed ω -lattice mechanism, the $\{112\}\langle 111\rangle$ -type twins nucleate inside nanoscale ω particles and grow out into bcc matrix. Therefore, the ω phase might act as a precursor phase prior to the formation of martensitic twins. The curved and overlapped twin boundary (Fig. 1) could be closely associated with the ω phase on the twin boundary (see Fig. 1 in ref. 53). Thus, the ω phase might play a crucial role in the martensitic transformation, and the ω lattice mechanism could be helpful to the development of the mechanism for martensitic transformation in steels.

Yonemura *et al.*⁵⁴ investigated the structural change of Fe-C steels when quenched (at approximately 100 K/s) from the molten state by using a time-resolved X-ray diffraction technique with intense synchrotron radiation; they found that fcc-to-bcc phase transformation occurs at a temperature far above the conventionally acknowledged M_s temperature. Sherby *et al.*⁵⁵ proposed that a martensitic transformation in carbon steels might take place in two steps—i.e., the formation of a primary martensite and secondary martensite. The primary martensite forms following a sequence in which the fcc austenite first transforms to a hexagonal structure and then to bcc martensite plus C-rich phase. In addition, a “pre-martensite” formed above nominal M_s was also proposed by Cayron⁵⁶, who believes that during martensitic transformation, the fcc matrix first transforms to a hexagonal close-packed phase and then to a bcc product⁵⁶. In the present study, we demonstrate that the intermediate phase is in a $P6_3/mmm$ hexagonal structure rather than a $P6_3/mmc$ hexagonal close-packed structured phase. The recent first-principles calculation and crystal structure analysis results added further weight to the proposal^{25,26}. The confirmation of the ω phase in carbon steels appears to be helpful to explicating the physical mechanism for the martensitic transformation in steels and to further improving the design of advanced martensitic steels.

In summary, an intensive TEM investigation has indicated that the extra diffraction spots frequently observed in martensitic carbon steels—which were historically ascribed to the diffraction from either internal twins or carbides—can be attributed to the ω phase, a metastable phase in particle-like morphology with overall size at the nanometre scale. The ω phase, with a hexagonal structure ($P6_3/mmm$) of $a_\omega = \sqrt{2} \times a_{\text{bcc}}$, $c_\omega = \sqrt{3}/2 \times a_{\text{bcc}}$, possesses strict orientation relationships with matrix ferrite as follows: $[\bar{1}13]_{\text{bcc}} // [\bar{1}\bar{1}23]_\omega$, $(110)_{\text{bcc}} // (\bar{1}011)_\omega$, $(2\bar{1}1)_{\text{bcc}} // (1\bar{1}00)_\omega$, which are in agreement with the relationships observed in other bcc metals and alloys.

Methods

Specimens 0.5 mm thick were cut from commercial carbon-steel bars with 0.58% C and 0.98% C (mass). The detailed chemical compositions of the specimens and their calculated martensitic transformation starting temperatures (M_s) are given in Table 1. All specimens were sealed in a quartz tube under an Ar atmosphere and austenitized for 30 min at 1373 K before quenching into brine. Specimens for TEM observation were prepared in a conventional way and finished by electropolishing in a twin-jet electropolisher with a chemical solution of 10% HClO_4 and 90% ethanol at 253 K. The microstructural observation was made with a JEM 2000FX TEM operated at 200 kV and a JEM 2100F high-resolution TEM operated at 200 kV. Electron diffraction patterns of the $\{112\}\langle 111\rangle$ -type twin structure were calculated using the software application xHREM (HREM Research Inc.).

References

- Bhadeshia, H. K. D. H. & Honeycombe, R. W. K. *Steels Microstructure and Properties* 3rd Ed, Ch. 5, 95–126 (Elsevier, Amsterdam, 2006).
- Delaey, L. *Phase transformations in materials*, (ed. Kostorz, G.) Ch. 9, 583–654 (WILEY-VCH Verlag GmbH, Weinheim, 2001).
- Aaronson, H. I., Enomoto, M. & Lee, J. K. *Mechanisms of diffusional phase transformations in metals and alloys*, Ch. 8, 622–632 (CRC Press, Boca Raton, 2010).
- Kelly, P. M. *Phase transformations in steels: diffusionless transformations, high strength steels, modelling and advanced analytical techniques*, (eds. Pereloma, E. & Edmonds, D. V.) Ch. 1, 4–23 (Woodhead Publishing, Cambridge, 2012).
- Kelly, P. M. Crystallography of lath martensite in steels. *Mater. Trans. JIM* **33**, 235–242 (1992).
- O'Neill, H. Twinning in alpha iron. *Nature* **135**, 1076–1077 (1935).
- Greninger, A. B. Twinning in alpha iron. *Nature* **135**, 916–917 (1935).
- Kelly, P. M. & Nutting, J. The martensite transformation in carbon steels. *Proc. Roy. Soc. A* **259**, 45–58 (1960).
- Crocker, A. G. Twinned martensite. *Acta Metall.* **10**, 113–122 (1962).
- Christian, J. W. & Mahajan, S. Deformation twinning. *Prog. Mater. Sci.* **39**, 1–157 (1995).
- Lee, H. Y. *et al.* Substructures of martensite in Fe-1C-17Cr stainless steel. *Scr. Mater.* **62**, 670–673 (2010).
- Stormvinter, A., Hedström, P. & Borgenstam, A. A transmission electron microscopy study of plate martensite formation in high-carbon low alloy steels. *J. Mater. Sci. Technol.* **29**, 373–379 (2013).
- Gates, J. D., Atrens, A. & Smith, I. O. Microstructure of as-quenched 3.5 NiCrMoV rotor steel - part II. Double diffraction. *Z. Werkstofftech.* **18**, 179–185 (1987).
- Bullough, R. & Wayman, C. M. Twinning and some associated diffraction effects in cubic and hexagonal metals: I-“selection rules” for twinning in fcc, bcc, and hcp lattice. *Trans. TMS AIME* **236**, 1704–1710 (1966).
- Wayman, C. M. & Bullough, R. Twinning and some associated diffraction effects in cubic and hexagonal metals: II-Double Diffraction. *Trans. TMS AIME* **236**, 1711–1715 (1966).
- Baker, T. N. Twins in iron alloys containing vanadium. *Acta Metall.* **21**, 261–266 (1973).
- Padmanabhan, R. & Wood, W. E. Occurrence of blocky martensite in 300M steel. *Mater. Sci. Eng.* **66**, 1–11 (1984).
- Li, S. *et al.* Experimental verification of segregation of carbon and precipitation of carbides due to deep cryogenic treatment for tool steel by internal friction method. *Mater. Sci. Eng. A* **575**, 51–60 (2013).
- Srinivasan, G. R. & Wayman, C. M. Transmission electron microscope study of the bainite transformation in iron-chromium-carbon alloys. *Acta Metall.* **16**, 609–620 (1968).
- Li, J. C., Chen, P. P. & Eaton, H. C. A new method for the simulation of electron diffraction patterns: the algorithm and its application to previous studies. *Scr. Metall.* **21**, 561–566 (1987).
- Ping, D. H. & Geng, W. T. A popular metastable omega phase in body-centered cubic steels. *Mater. Chem. Phys.* **139**, 830–835 (2013).
- Sikka, S. K., Vohra, Y. K. & Chidambaram, R. Omega phase in materials. *Prog. Mater. Sci.* **27**, 245–310 (1982).
- Silcock, J. M. An X-ray examination of the ω phase in TiV, TiMo and TiCr alloys. *Acta Metall.* **6**, 481–493 (1958).
- Sass, S. L. The ω phase in a Zr-25at.%Ti alloy. *Acta Metall.* **17**, 813–820 (1969).
- Togo, A. & Tanaka, I. Evolution of crystal structures in metallic elements. *Phys. Rev. B* **87**, 184104 1–6 (2013).
- Ping, D. H. Understanding solid-solid (fcc \leftrightarrow ω + bcc) transition at atomic scale. *Acta Metall. Sin. (Engl. Lett.)* **28**, 663–670 (2015).
- Zhu, Y. T., Liao, X. Z. & Wu, X. L. Deformation twinning in nanocrystalline materials. *Prog. Mater. Sci.* **57**, 1–62 (2012).
- Burbank, R. D. & Heidenreich, R. D. Microtwinning in epitaxial nickel-iron films. *Philos. Mag.* **5**, 373–382 (1960).
- Pashley, D. W. & Stowell, M. J. Electron microscopy and diffraction of twinned structures in evaporated films of gold. *Philos. Mag.* **8**, 1605–1632 (1963).
- Jack, D. H. & Jack, K. H. Invited review: carbides and nitrides in steel. *Mater. Sci. Eng.* **11**, 1–27 (1973).
- Senior, B. A. A critical review of precipitation behavior in 1CrMoV rotor steels. *Mater. Sci. Eng. A* **103**, 263–271 (1988).
- Tirumalasetty, G. K. *et al.* Novel ultrafine Fe(C) precipitates strengthen transformation induced plasticity steel. *Acta Mater.* **60**, 7160–7168 (2012).
- Jack, K. H. Structural transformations in the tempering of high-carbon martensitic steels. *J. Iron Steel Inst.* **169**, 26–36 (1951).
- Wells, M. G. H. An electron transmission study of the tempering of martensite in an Fe-Ni-C alloy. *Acta Metall.* **12**, 389–399 (1964).
- Bhadeshia, H. K. D. H. & Honeycombe, R. W. K. *Steels Microstructure and Properties* 3rd Ed, Ch. 9, 183–207 (Elsevier, Amsterdam, 2006).
- Ping, D. H. *et al.* Microstructural evolution in 13Cr-8Ni-2.5Mo-2Al martensitic precipitation-hardened stainless steel. *Mater. Sci. Eng. A* **394**, 285–295 (2005).
- Kruml, T., Polak, J. & Degallaix, S. Microstructure in 316LN stainless steel fatigued at low temperature. *Mater. Sci. Eng. A* **293**, 275–280 (2000).
- Huang, C. X. *et al.* Investigation on the nucleation mechanism of deformation-induced martensite in an austenitic stainless steel under severe plastic deformation. *J. Mater. Res.* **22**, 724–729 (2007).
- Morito, S. *et al.* The morphology and crystallography of lath martensite in alloy steels. *Acta Mater.* **54**, 5323–5331 (2006).
- Stormvinter, A. *et al.* Effect of carbon content on variant pairing of martensite in Fe-C alloys. *Acta Mater.* **60**, 7265–7274 (2012).
- Cayron, C. *et al.* Odd electron diffraction patterns in silicon nanowires and silicon thin films explained by microtwins and nanotwins. *J. Appl. Cryst.* **42**, 242–252 (2009).
- Frost, P. D. *et al.* Isothermal transformation of titanium chromium alloys. *Trans. Amer. Soc. Metals* **46**, 1056–1074 (1954).
- Hatt, B. A., Roberts, J. A. & Williams, G. I. Occurrence of the meta-stable omega phase in zirconium alloys. *Nature* **180**, 1406 (1957).
- Hatt, B. A. & Roberts, J. A. The ω -phase in zirconium base alloys. *Acta Metall.* **8**, 575–584 (1960).
- Hickman, B. S. The formation of omega phase in titanium and zirconium alloys: a review. *J. Mater. Sci.* **4**, 554–563 (1969).
- Cheng, G. M. *et al.* Deformation-induced ω phase in nanocrystalline Mo. *Scr. Mater.* **68**, 130–133 (2013).
- Delaey, L., Perkins, A. J. & Massalski, T. B. Review: on the structure and microstructure of quenched beta-brass type alloys. *J. Mater. Sci.* **7**, 1197–1215 (1972).
- Prasetyo, A., Reynaud, F. & Warlimont, H. Omega phase in quenched β brass and its relation to elastic anomalies. *Acta Metall.* **24**, 1009–1016 (1976).
- Hsiung, L. M. & Lassila, D. H. Shock-induced deformation twinning and omega transformation in tantalum and tantalum-tungsten alloys. *Acta Mater.* **48**, 4851–4865 (2000).
- Yedernal, A. F. & Perkas, M. D. Formation of a metastable ordered omega phase on ageing of the martensite in an Fe-Ni-Co-Mo alloy. *Phys. Met. Metallogr.* **33**, 89–97 (1972).
- Ayer, R., Bendel, L. P. & Zackay, V. F. Metastable precipitate in a duplex martensite ferrite precipitation-hardening stainless steel. *Metall. Trans. A* **23A**, 2447–2453 (1992).
- Ping, D. H. Review on ω phase in body-centered cubic metals and alloys. *Acta Metall. Sin. (Engl. Lett.)* **27**(1), 1–11 (2014).

53. Wu, S. Q. *et al.* {112}<111> Twinning during ω to body-centered cubic transition. *Acta Mater.* **62**, 122–128 (2014).
54. Yonemura, M. *et al.* Two-dimensional time-resolved X-ray diffraction study of directional solidification in steels. *Mater. Trans.* **47**, 2292–2298 (2006).
55. Sherby, O. D. *et al.* Revisiting the structure of martensite in iron-carbon steels. *Mater. Trans.* **49**, 2016–2027 (2008).
56. Cayron, C., Barcelo, F. & Carlan, Y. The mechanisms of the fcc–bcc martensitic transformation revealed by pole figures. *Acta Mater.* **58**, 1395–1402 (2010).
57. Payson, P. & Savage, C. H. Martensite reactions in alloy steels. *Trans. ASM* **33**, 261–275 (1944).
58. Stormvinter, A., Borgenstam, A. & Ågren, J. Thermodynamically based prediction of the martensite start temperature for commercial steels. *Metall. Mater. Trans. A* **43A**, 3870–3879 (2012).

Acknowledgements

Financial support was provided by the National Natural Science Foundation of China (No. 51271200 and No. 51471017) and Science Foundation of China University of Petroleum, Beijing. Part of the work was supported by the grant of JSPS KAKENHI 15H02304.

Author Contributions

T.W.L., D.X.Z. and Q.L. contributed to the experimental work. J.Y. contributed to the steel preparation. Y.J.Z., Y.J.S., X.Q.Z. and D.H.P. contributed to the result analysis and manuscript writing. M.S. contributed to the diffraction calculation.

Additional Information

Competing financial interests: The authors declare no competing financial interests.

How to cite this article: Liu, T. *et al.* A new nanoscale metastable iron phase in carbon steels. *Sci. Rep.* **5**, 15331; doi: 10.1038/srep15331 (2015).



This work is licensed under a Creative Commons Attribution 4.0 International License. The images or other third party material in this article are included in the article's Creative Commons license, unless indicated otherwise in the credit line; if the material is not included under the Creative Commons license, users will need to obtain permission from the license holder to reproduce the material. To view a copy of this license, visit <http://creativecommons.org/licenses/by/4.0/>